Russian Chemical Reviews **82** (11) 1066 – 1080 (2013) © 2013 Russian Academy of Sciences and Turpion Ltd

DOI 10.1070/RC2013v082n11ABEH004373

New insight into the spreading dynamics of liquids on rough surfaces using computational fluid dynamics

H Alla, S Freifer, B A Talha, T Roques-Carmes

Contents

I.	Introduction	1066
II.	Choice of the simulation method	1067
III.	Implementation of the computational fluid dynamics model	1068
IV.	Numerical parameters	1071
V.	Comparison of the modelling results with experimental data	1072
VI.	Conclusion	1079

Abstract. The potential of modelling of liquid drop spreading on a rough surface by various approaches is analyzed. A number of examples (silicone oil on glass, mineral oil on stainless steel, *etc*.) are used to demonstrate good agreement between the results obtained by computational fluid dynamics and experimental data. The effects of various parameters (surface characteristics, properties of the liquid) on the process of spreading and the possibility to take account for these factors in the modelling are considered. Data on different spreading mechanisms on rough surfaces are presented. The bibliography includes 69 references.

I. Introduction

The dynamics of spreading is a very active area of research, not only for purely scientific reasons but also because many industrial and material processing operations require the spreading of liquid on a solid. To name just a few, we mention surface coating, printing, painting, and processes in trickle bed reactors, packed beds, structured reactors and monoliths. Although wetting has been studied for many years,[1,2] many fundamental problems remain open, especially those related to the motion kinetics of the contact-line, particularly, on rough surfaces.[3,4,5] However, most practical solid surfaces are rough to some extent, and for some applications of wetting, roughness of the surface may even be essential. Because the involved phenomena are complex, our understanding of the drop spreading on rough surfaces remains limited. Thus the present-day ability to predict the dynamics of wetting and to model processes that are dependent on wetting on rough surfaces is still significantly restricted.[2]

It becomes then necessary to develop a numerical tool in order to simulate the complex hydrodynamics of wetting on rough surfaces. Several numerical methods of computational fluid dynamics (CFD) are available to simulate free-surface flows (flows with moving interfaces). The volume of fluid technique (VOF) is one of the most widely used methods in modelling of free surfaces.[6–10] This is a fixed-mesh method, in which the interface between immiscible fluids is modelled as the discontinuity in a characteristic function (such as volume fraction). Nichita *et al*.[11,12] successfully developed a dynamic contact angle model into the VOF method to simulate the dynamics of spreading of a water drop on a smooth coated silicon wafer surface. This model accounted fairly well for the experimental spreading behaviours observed for large drops for which gravity cannot be neglected. In the same way, Gunjal *et al*.[13,14] applied a similar CFD/VOF approach to simulate the process of spreading/recoiling of a liquid drop after collision with a flat smooth solid surface at relatively high impact velocities (the Reynolds numbers based on drop impact velocity were 550 to 2500). The simulations showed reasonably good agreement with the experimental data for the water/Teflon system. Recently, we have adapted these CFD/VOF models to simulate the dynamics of spreading in the case of a drop previously deposited on a surface.[15] We studied the spreading of glycerol – water mixtures with and without a surfactant on smooth hydrophilic glass surfaces for a large range of viscosity (0.02 – 1.15 Pa s), surface tension (29 – 64 mN m^{-1}) and drop volume (8 – 60 μl). A very good agreement with experimental data was reported.[15] However, simulations by computational fluid dynamics of drops spreading over rough surfaces, for which the details of surface geometry must be resolved, pose major challenges. The approach developed by Natarajan and Hangan[16] is of particular interest for the spreading on rough surfaces. They implemented a CFD model in order

H Alla, S Freifer, B A Talha Université des Sciences et de la Technologie d'Oran, BP 1505 El M'Naouar Bir el Djir 31000, Oran, Algeria.
E-mail: houcine_alla@yahoo.fr (H Alla), f.somia@yahoo.fr (S Freifer), a.t_badra@yahoo.fr (B A Talha);
T Roques-Carmes Université de Lorraine, Laboratoire Réactions et Génie des Procédés, CNRS, UMR 7274 CNRS, Nancy, F-54000, France.
Tel. (33 383) 17 50 89, e-mail: thibault.roques-carmes@univ-lorraine.fr

Received 1 February 2012
Uspekhi Khimii **82** (11) 1066 – 1080 (2013)

to address the effect of surface roughness on tornado-like flows. The roughness was introduced in the simulation as an equivalent sand-grain roughness. The roughness was expressed by means of wall functions applied to the bottom of the computational domain.[17] This type of roughness modification is currently present in many CFD codes. The predictions of the velocity vectors, pressure deficit and core radius were in good agreement with experimental data during the numerical study of the effects of surface roughness on tornado-like vortices. However, no information is available about the validity of this 'roughness' approach for the VOF method and more particularly in the case of the spreading of drops on rough surfaces.

It is also essential to provide a large amount of experimental data in order to validate and guide the development of this numerical model. The experimental study of spreading on practical rough surfaces is difficult, because the problem of defining roughness is complex. For this reason, much work has been done on spreading on surfaces with well-defined grooves or roughness.[18–21] Nonetheless, some measurements of the kinetics of spreading of liquids on practical rough surfaces were also made.[22–27] These latter studies show that a rich set of behaviours can be obtained by varying the surface pattern and the wetting properties of the liquid. On the one hand, Cazabat and Cohen Stuart [22, 23] explored experimentally the dynamics of spreading of silicone oils on rough glass surfaces (roughness height range of 2 μm to 50 μm). This study revealed that the spreading of the liquid occurs by two modes: on top of the rough surface and inside the capillary grooves which make up the roughness (Wenzel state). On the other hand, Narayan Prabhu *et al.*[24] have experimentally studied the dynamics of drop spreading of mineral and vegetable oils on stainless steel surfaces for substrate roughness heights ranging from 0.5 to 2 μm. They showed that the liquid was only in contact with the upper part of the relief during the spreading process (Cassie state). In other words, the spreading of the liquid occurred by only one mode: on the top of the rough surface.

To this extent, the simulated results can be compared with the experimental data reported by Narayan Prabhu *et al.*[24] and Cazabat and Cohen Stuart.[22, 23] These two typical cases have been selected to illustrate the model. The aim of this article is to verify the validity of the model mentioned above, over rather long time periods (more than 10^5 s), for the different spreading regimes that are observed with a large range of surface wetting characteristics, liquid properties and roughness sizes.

II. Choice of the simulation method

Numerical modelling of contact-line motion is difficult because of the widely differing length scales involved in the problem. Several numerical studies on the dynamics of liquid drop spreading over solid surfaces have been reported in the literature.[11–15] In the following, the main computer simulation methods, including computational fluid dynamics (CFD), lattice Boltzmann (LB), and molecular dynamics (MD), are briefly reviewed.

The lattice Boltzmann method is based on a minimal form of the Boltzmann kinetic equation describing the time evolution of discrete particle distribution function $f_i(x,t)$, denoting the probability of finding a particle at lattice site x and time t moving along the lattice vector $\mathbf{c}_i$, where the index i labels the discrete directions of motion. It is necessary to introduce an additional interaction force between the wall and the liquid responsible for surface wettability.[28–30] This extra force is acting in all cells of the interface between the wall and the liquid, and produces artificial density distributions in the liquid near the interface.[31, 32] In addition, there is no unambiguous correlation between the strength of the interaction force and the wetting angle, *i.e.*, the interaction force has to be adjusted when the size of the drop is changed.[33]

Molecular dynamics is one of the few tools available to explore the molecular details of wetting. However, it is only within the last 25 years that computer power has grown sufficiently to make it practical to compute the dynamics of quasi macroscopic systems and then simulate a real experiment.[34–37] Molecular dynamics has been extensively used to shed more light on molecular processes close to the contact-line region.[38, 39] In the MD simulations, the fluid particles interact with each other through a Lennard-Jones potential. The obvious strength of the technique in the study of dynamic wetting is that it can delve into the process at the molecular level. Another advantage is that it can provide a level of control that would be impossible to achieve in wetting experiments. The appealing feature of MD is that it follows the actual dynamical evolution of the system. On the negative side, the simulations are still restricted to small systems of the order of a few tens of nanometres and short times of the order of a few nanoseconds. The simulations are also subject to significant thermal and statistical fluctuations. In addition, MD models can also provide useful information on the local boundary conditions but they remain valid only for specific situations and none of them can satisfy all cases.

In principle, continuum fluid mechanics (CFD) provides the most economical description of microflows. However, this approach fails to describe a series of phenomena such as near-wall slip-flow in which the continuum assumption is under question because of the onset of molecular effects, especially near solid walls. MD provides a high degree of physical fidelity at the price of a very substantial computational burden. The lattice kinetic approach is well positioned to offer a good compromise between the physical realism of molecular dynamics and the computational efficiency of continuum mechanics. The LB method finds increasing applications in microfluidic problems because it allows the handling of fluid-wall interactions at a more microscopic level than do the Navier–Stokes equations while simultaneously reaching much larger scales than MD.[40, 41] However, the LB approach is subject to a number of limitations, such as the existence of spurious currents near curved interfaces as well as enhanced evaporation/condensation effects due to the finite width of the interface.[42] Although the CFD method is well suited to handle complex geometries, it also shows some physical and computational limitations, namely, anomalous long transients and the need for a large computational grid to ensure the required accuracy, which entails a correspondingly long computational time, which is much closer to the MD requirements than to the LB ones. By construction, the CFD approach is able to reproduce exactly all of the physical properties of the flow while both LB and MD show some discrepancies in the values of the surface tension and vapour density. These discrepancies render them irrelevant for the investigation of the macroscopic features of capillary imbibition.[43]

A detailed comparative assessment of the merits and disadvantages of the three levels of description is therefore of great importance in the ultimate goal of developing efficient, robust multiscale coupling methods for complex microfluidic flows. In a previous work, Chibbaro *et al.*[44] presented a comparative study of capillary filling in the presence of wall corrugations, using all the methods mentioned above (CFD, LB and MD). The numerical results of these approaches were compared and tested against the Concus–Finn (CF) criterion, which predicted pinning of the contact-line at rectangular ridges perpendicular to flow for contact angles larger than 45°. All the three methods exhibited satisfactory agreement with the experimental results, although on a different range of timescales. Whereas the pinning of the liquid front was observed in the LB and CFD simulations, MD calculations showed that molecular fluctuations allowed front propagation even above the critical value predicted by the deterministic CF criterion, thereby introducing a sensitivity to the obstacle height.

In summary, none of the above discussed approaches can be used as general numerical solution for dynamic wetting problems. It is obvious that the available methods for wetting simulation display limitations. Ideally, one would combine the three methods within a synergistic multiscale procedure, using each of them wherever/whenever appropriate in different regions of the microflow. In the following, the volume of fluid method (CFD/VOF) will be used for the simulation of drop spreading on rough surfaces since it is still the most preferred method for the computations of drop impact and spreading where strong topological changes of interfaces occur.[8, 13]

III. Implementation of the computational fluid dynamics model

1. Model equations

We study the time evolution of a sessile liquid drop, which is initially placed (at time $t = 0$) on an horizontal rough solid substrate exposed to air in a nonequilibrium configuration and then evolves towards its equilibrium shape.

We first introduce the solution domain and the computational grids. A three-dimensional domain is considered to carry out simulations of drop spreading. To minimize demands on computational resources, without jeopardizing the ability to capture key features, the solution domain for such 3D simulations is restricted to 90° with two planes of symmetry (instead of the full 360°). The axisymmetric solution domain is shown in Fig. 1 *a*. The computational grid is generated using GAMBIT software. A uniform grid is used in the whole domain. The computational domain is mapped with structured square meshes of constant size (Δx).

The volume of fluid approach (VOF), with piecewise linear interface calculations method (PLIC) for interface reconstruction, is used to simulate the liquid/gas interface and also the drop spreading on the solid surface. A VOF interface tracking method is adopted to represent the fluid domain and track the evolution of the domain's free boundaries. Gas and liquid phases are considered to be incompressible, laminar and Newtonian fluids with constant values of viscosity and surface tension. The continuum surface force technique (CFS), is applied to model surface forces and surface adhesion.[45]

The mass and momentum conservation equations for each phase read as

$$\nabla \cdot \mathbf{u} = 0 \tag{1}$$

$$\frac{\partial \mathbf{u}}{\partial t} + \nabla \cdot (\mathbf{u}\,\mathbf{u}) = -\frac{1}{\rho}\left(\nabla P - \mu \nabla^2 \mathbf{u}\right) + g + \frac{1}{\rho}\mathbf{F}_{\mathrm{SF}} \tag{2}$$

where $\mathbf{u}$ represents the velocity vector, P is pressure, μ is dynamic viscosity, ρ is density, g is the gravitational acceleration, ∇ is vector differential Del operator, and $\mathbf{F}_{\mathrm{SF}}$ is the continuum surface force vector due to the surface tension. This single set of flow equations is utilized throughout the domain and mixture properties as defined below are used.

A scalar parameter of F is defined to mean the fraction of the volume of each computational cell in the grid that is occupied by the liquid.[6] The volume fraction of gas is by definition $1-F$. Thus, F takes the value one in cells that contain only liquid and the value zero in cells that contain only air. A cell that contains the gas/liquid interface would have an F value between zero and one (Fig. 1 *a*).

The density and the dynamic viscosity of the mixture are calculated as

$$\rho = \rho_{\mathrm{L}} + (\rho_{\mathrm{G}} - \rho_{\mathrm{L}})F \tag{3}$$

$$\mu = \mu_{\mathrm{L}} + (\mu_{\mathrm{G}} - \mu_{\mathrm{L}})F \tag{4}$$

where the subscripts L and G denote liquid and gas phases, respectively.

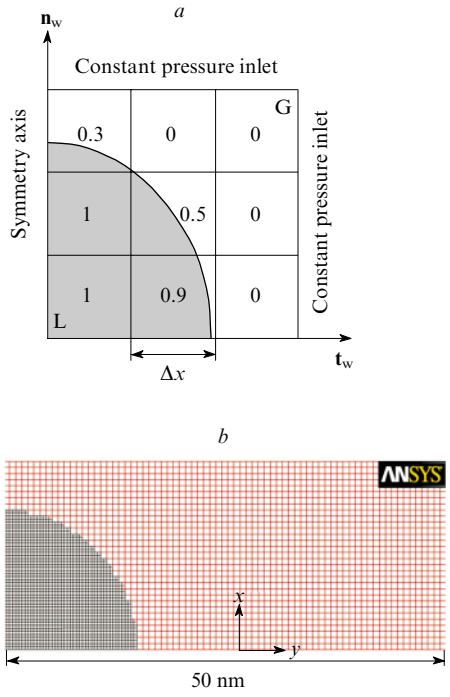


Figure 1. Schematic diagram of the free-surface reconstructions: (*a*) Actual interface: the exact VOF colour function for a circular arc over a square grid. The figure also contains the solution domain and boundary conditions. (*b*) Interface reconstruction with PLIC method. The number of cells is reduced compared to those used in the actual simulation for clarity reasons.

The manner in which the volume fraction distribution F (and hence the distribution of liquid) evolves is determined by solving the passive transport equation

$$\frac{\partial F}{\partial t} + \mathbf{u} \cdot \nabla F = 0 \tag{5}$$

In addition to the mass and momentum balance equations, surface tension and wall adhesion must be accounted for. Surface tension is modelled as a smooth variation of capillary pressure across the interface. Although representing the surface force in the form of volumetric source terms, stresses arriving as a result of a gradient in the surface tension are neglected. Following Brackbill *et al.*,[45] it is represented as a continuum surface force ($\mathbf{F}_{SF}$) and is specified as a source term in the momentum equation as

$$\mathbf{F}_{SF} = \gamma \frac{\rho \alpha \nabla F}{1/2(\rho_G + \rho_L)} \tag{6}$$

where γ is the liquid/gas surface tension and α is the curvature of the interface calculated as

$$\alpha = \frac{1}{|\mathbf{n}|}\left[\left(\frac{\mathbf{n}}{|\mathbf{n}|} \cdot \nabla\right)|\mathbf{n}| - (\nabla \cdot \mathbf{n})\right] \tag{7}$$

The normal vector to the surface $\mathbf{n}$ is estimated in the cells that contain the liquid/gas interface and requires the knowledge of the volume of fluid present in the cell.

Surface reconstruction is a prerequisite for determining the flux of liquid from one cell to the next, and surface curvatures when the surface tension model is activated. The VOF algorithm solves the problem of updating the volume fraction field F given the fixed grid, the velocity field and the field F at the previous step. In this scheme, a straight-line segment approximates an interface within a computational cell. The interface is considered to be a continuous piecewise smooth line, and the problem of its reconstruction is that of finding the approximation to the section of the interface in each cell, by knowing only the volume fraction F in that cell and in the neighbouring cells. The VOF technique based on piecewise linear interface calculation (PLIC) attempts to fit the interface with piecewise linear segments.[46, 47] Figure 1 *a* shows the exact VOF function for a smooth circular arc. Figure 1 *b* exhibits an interface reconstructed with VOF/PLIC. Note that the number of cells depicted in the Figure is reduced for clarity reasons. Since F in Eqn (5) is not a continuous function, the VOF/PLIC algorithm is divided into two parts: a reconstruction step (i) and a propagation step (ii). The reconstruction step (i) allows the determination of the orientation of the segment. This is equivalent to the determination of the unit normal vector $\mathbf{n}$ to the segment. The normal vector $\mathbf{n}$ and the volume fraction F then uniquely determine the straight line. The propagation step (ii) is done using a fractional step or an operator split method, which updates the volume fraction F along one spatial direction at a time.

Wall adhesion is included in the model through the contact angle. For fluids exhibiting a nonzero contact angle, the presence of wall also affects the surface normal and therefore wall adhesion forces are included in the present work. The wall adhesion is modelled in a manner similar to that of the surface tension in the case of a gas/liquid interface,[45] except that the unit normal $\mathbf{n}$ in this case is determined using the contact angle θ_d according to

$$\mathbf{n} = \mathbf{n}_w \cos\theta_d + \mathbf{t}_w \sin\theta_d \tag{8}$$

where $\mathbf{n}_w$ and $\mathbf{t}_w$ are the unit vectors normal and tangential to the wall (see Fig. 1 *a*), respectively, and θ_d is the dynamic contact angle at the wall. Surface normal obtained from one cell above the wall and near the wall [from Eqn (8)] are used to obtain the body surface force from the surface tension. Several models describe the evolution of the contact angle of the fluid. One approach is to assign a constant value to the equilibrium contact angle θ_d neglecting the contact angle hysteresis. This is also referred to as a static contact angle model. An alternative way is the application of a varying value of the contact angle, which depends on instantaneous flow parameters. These models are called dynamic contact angle models. One of the most recent and accurate ones is the Kistler model,[48] which calculates the dynamic contact angle θ_d using the Hoffman function f_{Hoff} as follows

$$\theta_d = f_{Hoff}\left[\frac{U_{cl}\,\mu}{\gamma} + f_{Hoff}^{-1}(\theta)\right] \tag{9}$$

where θ is the equilibrium contact angle, f_{Hoff}^{-1} is reciprocal of the Hoffman function (f_{Hoff}), U_{cl} is the spreading velocity of the contact-line, μ is the dynamic viscosity of the liquid and γ is the surface tension at the liquid/gas interface. The Hoffman function f_{Hoff} is defined as

$$f_{Hoff}(x) = \arccos\left\{1 - 2\mathrm{th}\left[5.16\left(\frac{x}{1 + 1.31x^{0.99}}\right)^{0.706}\right]\right\} \tag{10}$$

Equation (9) shows that the dynamic contact angle θ_d depends on the spreading velocity of the contact-line and requires the input of an equilibrium contact angle. For surfaces which are not smooth, the equilibrium angle θ is replaced by either a limiting advancing or receding contact angle θ_a or θ_R, respectively, depending on the sign of the velocity U_{cl} of the contact-line. This model is then modified with the implementation of the advancing angle θ_a if the contact-line has a positive velocity (spreading) and the receding angle θ_R if the contact-line has a negative velocity (receding). For the dynamic model the Kistler approach is adopted with limiting advancing and receding contact angles measured experimentally. To this extent, we use the experimental data reported by Narayan Prabhu *et al.*[24] and Cazabat and Cohen Stuart.[22, 23]

2. Boundary conditions

In this part, we discuss the relationship between the boundary conditions and the roughness of the surface taking into account the wetting properties (hydrophobic/hydrophilic) of the textured surface. The phenomenon of slip refers to any situation in the dynamics of fluids where the value of the tangential component of the velocity appears to be different from that of the solid surface in contact with it. The slip length is defined as the distance within the solid at which the flow profile extrapolates to zero.

In recent years, it has become clear that the no-slip boundary condition at the solid/liquid interface is only valid for smooth hydrophilic surfaces.[49 – 51] Thus, the hydrophobicity of smooth surfaces could induce a partial slip-

page.[49, 50, 52, 53] In this case, the slip length can be of the order of tens of nanometres.[49] The behaviour becomes different with rough surfaces.[54] The value of the slip length is significantly affected by the nature of the rough surface. The flow of poorly wetting liquids on the topography of the surface favours the formation of trapped air bubbles within the texture (Cassie state). This configuration generates superhydrophobic slippage.[52, 53] More precisely, the slippage increases dramatically and slip lengths up to hundreds of micrometres may be attained.[53] For rough wettable surfaces in a Wenzel state, the situation remains ambiguous since opposite conclusions have been reached. Bonaccurso *et al.*[55] demonstrated that the roughness leads to large slip, while Granick *et al.*[56] claimed that the topography diminishes the extent of slippage. To summarize, the slippage and the slip length remain larger for drops in a Cassie state than for those in a Wenzel state.

Consequently, the flow boundary conditions (*i.e.*, the effective hydrodynamic boundary conditions) for rough surface depend significantly on the state of the drop on the surface. For Wenzel state, it appears necessary to use the effective no-slip boundary condition, which is applied at the imaginary smooth homogeneous isotropic surface located at an intermediate position between the top and bottom of grooves.[57] It is interesting to note that the position between the top and bottom of the roughness is affected by the density of the roughness element. Calculations based on this approach lead to an excellent description of the experimental data.[57] On the contrary, on hydrophobic solids in the Cassie state, the situation and the boundary conditions are different. The rough surface has to be considered as perfectly smooth with a pattern of boundary conditions: (i) no-slip condition on the top of the roughness (solid/liquid interface) and (ii) partial slip inside the roughness (gas/liquid region).[52] Using this concept, it appears that the calculated results are in good agreement with experimental data.[52]

In the present study we use a slightly different approach. The main advantage of our approach is that it does not depend on the state of the drop on the surface (Cassie or Wenzel state). Due to the importance of the surface roughness in the wetting behaviour of a drop on a surface, the use of wall functions is required for near-wall modelling inside the roughness in order to create an interaction between the liquid and the porosity (roughness), *i.e.*, the immersion of the liquid inside the roughness. This means that the wall function is necessary for the liquid to find 'navigable channels' inside the roughness. In the absence of wall function, the simulation is unable to pull the liquid inside the roughness. However, the wall function is a calculating tool without real physical meaning and is only used to initiate the flow of liquid inside the roughness.

There are a range of parameters which are reported to describe the roughness of a surface.[58, 59] The most common are the average roughness height and the peak-to-peak distance. While the experimental roughness created on the surfaces is random, numerical modelling with a well-defined roughness model can provide valuable information about the spreading behaviour of the drop.

Roughness effects are introduced in the CFD code by modifying the wall function which is based on the universal near-wall velocity distribution. In this section, the roughness modification that is based on experiments with sand-grain roughness is described. The modified wall function is given by[16, 17]

$$\frac{u_{\mathrm{p}}u^*}{\tau_{\mathrm{w}}/\rho} = \frac{1}{\kappa}\ln\left(E\rho x_{\mathrm{p}}\frac{u^*}{\mu}\right) - \Delta B \tag{11}$$

where u_{p} and x_{p} are the velocity and height to the surface (bottom of the domain) at the midpoint P of the wall adjacent cell. E represents an empirical constant for a smooth wall with a value of 9.793, τ_{w} is the wall shear stress, κ is the Von Kármán constant (~ 0.41), u^* is the wall friction velocity and ΔB is the roughness function.

The wall friction velocity u^* is defined as

$$u^* = C_{\mu}^{1/4}k_p^{1/2} \tag{12}$$

where k_{p} denotes the kinetic energy in the wall adjacent cell midpoint P and C_{μ} refers to a constant with default value of 0.09.

The roughness function ΔB depends on the type (uniform sand, rivets, threads, ribs, mesh-wire, *etc.*) and the size of the roughness. There is no universal roughness function valid for all types of roughness. The roughness is implemented in the simulation as an equivalent sand-grain roughness as discussed by Blocken and co-workers.[17] For a sand-grain roughness and similar types of uniform roughness elements, ΔB is defined as a function of the dimensionless sand-grain roughness height h^*. The dimensionless roughness height h^* is then defined by

$$h^* = \rho\frac{h_{\mathrm{r}}u^*}{\mu} \tag{13}$$

where h_{r} is the equivalent sand-grain roughness height. In the present case, we consider that h_{r} represents the physical roughness height.

Depending on the value of h^*, the roughness can be classified into three regimes.[16, 17] When $h^* < 2.25$, we deal with an aerodynamically smooth regime, while when h^* ranges between 2.25 and 90 it is a transitional regime. The fully rough regime is obtained for $h^* \geqslant 90$. The formula used for ΔB depends on the roughness regime. In the present study, the surface roughness height h_{r} ranges between 0.5 and 50 μm, which corresponds to $h^* < 2.25$. Consequently the wetting of the drop over the surface falls in the aerodynamically smooth regime. The roughness function ΔB corresponding to this regime is given by

$$\Delta B = \frac{1}{\kappa}\ln(C_{\mathrm{s}}h^*) \tag{14}$$

where C_{s} is the roughness constant, which takes into account the peak-to-peak distance. To summarize, the roughness is then introduced in the Fluent software by specifying the values of the roughness height h_{r} (average roughness height) and the roughness constant C_{s} (peak-to-peak distance) in the wall boundary conditions inside the roughness.

The other boundary conditions are discussed. Along the symmetry axis (x-axis in Fig. 1b) a symmetric boundary condition is imposed in which normal velocity and normal gradients are set to zero, *i.e.*, $u = 0$ and $\partial u/\partial x = 0$. A no-slip boundary condition is used at the wall on the top of the rough surface where all the components of velocity are set

to zero. Although the no-slip boundary condition (zero velocity on the wall) is implemented at the wall boundary on the top of roughness, the gas/liquid/solid contact-line moves along the wall, presenting a kind of singularity. Because velocity profiles at the other two planes (other than symmetry and wall planes) of the solution domain are not known, a constant pressure boundary condition is used at these planes (Fig. 1 *a*). The numerical treatment of a moving three-phase (gas/liquid/solid) contact-line requires further discussion. Slip is necessary for the translation of the contact-line of a drop on a solid surface. While a no-slip boundary condition is imposed for the fluid velocities at the solid surface, the moving contact-line feels a slip. In our CFD simulations, a no-slip boundary condition at the wall is then imposed. However, this does not mean that the contact-line with the wall cannot move, as the code integrates over the whole cell adjacent to the wall to compute the mass flux of the second phase, which, when using a finite grid size, will average out to give an apparent finite interface velocity at the wall. The numerical velocity of the element at the vicinity of the surface was already estimated and is typically in the range of a few nm per second.[51, 60] The numerically induced slip was also described by Renardy *et al.*[61] and Afkhami *et al.*,[62] who showed that the contact-line motion is not very sensitive to the addition of artificial slip lengths with magnitudes in the order of the grid size. In most of the applications, the slip length is expected to be much smaller than the mesh size used in the numerical computations. The available computational resources do not allow the mesh size to be refined in such a way that the true slip length is captured correctly. In the present work, therefore, no explicit slip length is imposed. However, it should be noted that the algorithm itself introduces the implicit slip length of the order of the grid spacing.

To summarize, the wall function is applied for near-wall modelling inside the roughness, while a no-slip boundary condition is used at the wall on the top of the rough surface. The model equations given above are solved using the commercial flow solver Ansys Fluent 12.0.16. The spatial derivatives in Eqns (1) and (5) are discretized using the quadratic upwind interpolation for convective kinetics system (QUICK) scheme while the temporal derivatives are discretized using a first-order implicit method. The pressure implicit with splitting of operator (PISO) scheme is used for the pressure velocity coupling in the momentum equation.

IV. Numerical parameters

Care is taken to ensure that the results are not influenced by the numerical parameters such as grid size, time step, and drop radius at time $t = 0$. One limitation of the CFD approach is the estimation of the initial drop radius and contact angle. It should be noted that any differences in initial conditions would amplify the discrepancy between simulated and experimental results as time progresses. The behaviour of a liquid drop after impact on a solid surface depends on impact velocity.[13] The aim of the present work is to study the spreading in the capillary regime, where inertial effects are small. For that reason, the spreading is studied in situations where the drops are gently contacted with the surface (drop impact velocity < 1 m s^{-1}). For the CFD model, the multiphase flow must be initialized so that the simulation starts from a stable initial position. Because it is impossible to specify the exact initial conditions corresponding to the experiments in the VOF simulations, all calculations are initiated with the experimental value of the initial radius.

In the analysis of the temporal evolution, it turns out that the dynamic behaviour is sensitive to details of the dynamic contact angle, which is related to mesh size (Δx) and time step size (Δt). An optimization between time step size and mesh size needs to be performed. The optimization principle is to find the larger mesh size which gives no variation between the numerical solutions obtained with different mesh sizes. In order to investigate the effect of the grid resolution, simulations are performed with mesh sizes ranging from 5×10^{-5} mm to 5×10^{-3} mm at a constant time step of 5×10^{-6} s. The simulations are made with a drop of silicone oil on a glass surface of roughness height equal to $h_r = 50$ μm and a peak-to-peak distance of 12 μm. Figure 2 represents the dependence of the time variation of the calculated base radius on mesh size. When using meshes of size of 8×10^{-4} mm and above, the dimension of the domain affects the calculated results. The mesh size is too high to ensure grid-independent results. As the mesh size increases, the simulated curves become somewhat steeper. However, all the curves reach a plateau at the same value. On the contrary, when using mesh sizes less than or equal to 5×10^{-4} mm, the calculated radii are not affected by the dimension of the meshes. For instance, simulations using $\Delta x = 5 \times 10^{-5}$ and 5×10^{-4} mm exhibit no variation between the simulation results. The trend is similar to that described by Afkhami *et al.*[62] for the CFD/VOF simulation of the spontaneous spreading of a drop at small capillary and Reynolds numbers, and Schönfeld *et al.*[63] for the CFD calculation of the capillary rise. All previous studies illustrate that the large friction in close vicinity to the three-phase contact-line is more accurately reproduced on finer meshes.[61 – 65] Therefore, a mesh size of 5×10^{-4} mm is used for all the simulations.

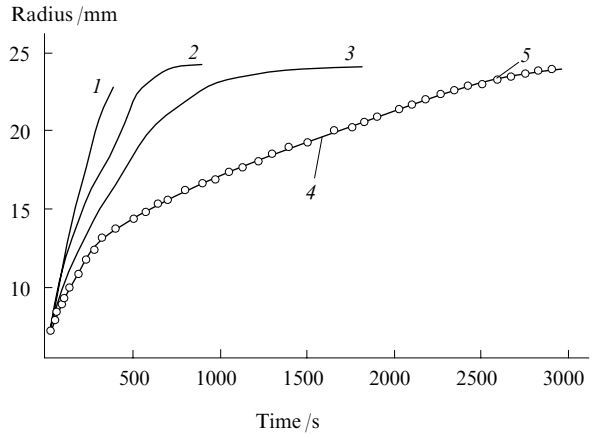


Figure 2. Mesh size optimization. Time evolution of the calculated drop radius of silicone oil on glass surface of roughness height equal to $h_r = 50$ μm for different mesh sizes (Δx). For $\Delta x = 5 \times 10^{-5}$ mm, the number of points (calculated radiuses) depicted in the figure is reduced for clarity reasons.
Δx /mm: 5×10^{-3} (*1*), 10^{-3} (*2*), 8×10^{-4} (*3*), 5×10^{-4} (*4*), 5×10^{-5} (*5*).
Parameters used in calculations: $\gamma = 24$ mN m^{-1}, $\mu = 0.02$ Pa s, $h_r = 50$ μm, peak-to-peak distance = 12 μm, and $\Delta t = 5 \times 10^{-6}$ s.

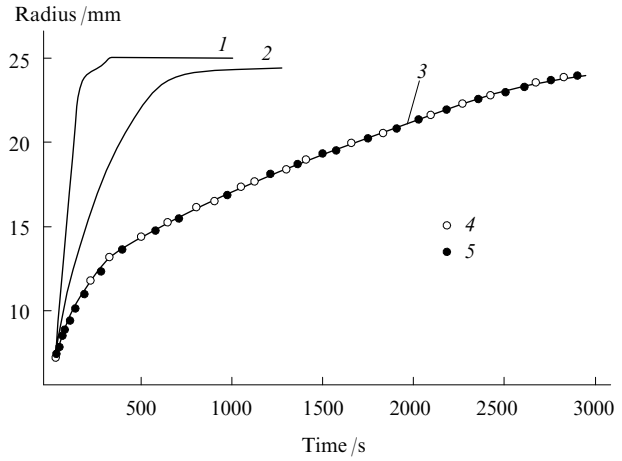


Figure 3. Time step size optimization. Time evolution of the drop radius of silicone oil on glass surface of roughness height equal to $h_r = 50$ μm for different time steps (Δt). For $\Delta t = 10^{-7}$ and 5×10^{-7} s, the number of points (calculated radii) depicted in the figure is reduced for clarity reasons.
Δt /s: 8×10^{-4} (*1*), 5×10^{-5} (*2*), 5×10^{-6} (*3*), 5×10^{-7} (*4*), 10^{-7} (*5*). Parameters used in calculations: $\gamma = 24$ mN m^{-1}, $\mu = 0.02$ Pa s, $h_r = 50$ μm, peak-to-peak distance = 12 μm, and $\Delta x = 5 \times 10^{-4}$ mm.

In order to identify the appropriate temporal discretization, several simulations are carried out with time steps (Δt) varying from 10^{-7} to 8×10^{-4} s using a constant computational grid size of 5×10^{-4} mm. The simulations are made with a drop of silicone oil onto a glass surface of roughness height of 50 μm and a peak-to-peak distance of 12 μm (Fig. 3). For time steps larger than or equal to 5×10^{-5} s, the CFD implementation leads to a time step dependence of the numerical results, mostly because dynamic changes of the contact angle and the (diverging) contact-line friction are more accurately captured on finer time steps. A time step of 5×10^{-6} s is found to adequately capture the key features of drop dynamics since the simulations using $\Delta t = 10^{-7}$, 5×10^{-7} and 5×10^{-6} s show no difference in the predicted results.

Note that the previous numerical optimizations (Δt and Δx) were performed using a surface with a very large roughness size ($h_r = 50$ μm and a peak-to-peak distance of 12 μm, see Figs 2 and 3). It is anticipated that the size of the roughness might affect the optimum values of the time step and mesh size. An optimization between time step size and mesh size needs to be performed for each roughness height. In our approach, the computational grid size remains constant ($\Delta x = 5 \times 10^{-4}$ mm) and simulations have been performed in order to identify the appropriate temporal discretization for each roughness size. Table 1 illustrates the values of the optimum time step for different roughness heights. The optimum time step displayed in the table is the maximum value of Δt in order to ensure time step-independent results. The roughness height influences the values of the optimum time step. Two ranges of roughness size can be identified. Within each of these ranges the time steps do not vary with the roughness dimension. The critical roughness height is equal to 2.4 μm. For roughness height lower than 2.4 μm, the Δt values are 10^{-5} s. However, for roughness size larger than or equal to 2.4 μm, a significant drop of Δt is reported. The optimum time step becomes $(2-5) \times 10^{-6}$ s. Finer time steps are required for high surface roughness due to the large friction in close vicinity of the surface. In fact, within a measured unit surface area on a rough substrate there is more surface in contact with the spreading liquid. This surface, in contact with the spreading liquid, increases with the roughness size.

Table 1. Optimum time steps for different roughness heights. The maximum time steps Δt that ensure time step size-independent results are presented.

Roughness height /μm	Type of oil	Optimum Δt /s
50	silicone	5×10^{-6}
18	"	3×10^{-6}
4.7	"	2×10^{-6}
2.4	"	3×10^{-6}
2	coconut, mineral, palm	10^{-5}
1	the same	10^{-5}
0.5	"	10^{-5}

V. Comparison of the modelling results with experimental data

1. Spreading of silicone oil on glass

Simulations of drop dynamics of silicone oil on glass of varying roughness are performed. The experimental data were previously reported by Cazabat and Cohen Stuart.[22,23] They allow us to test the validity of the model for a large range of roughness sizes (roughness height: 2.4 – 50 μm) and also over a very long period of time (140 000 s or 38 hours). The rough surfaces were obtained either by depolishing glass slides by means of various grades of abrasive powder (for fine roughness) or by sand blasting (for large roughness). The roughness heights (h_r) were 2.4, 4.7, 18 and 50 μm, respectively. The corresponding peak-to-peak distances were 0.4, 0.7, 3.6 and 12 μm, respectively. A silicone oil [methyl-terminated poly(dimethylsiloxane)] of viscosity of 0.02 Pa s, was used because it wets glass well (perfectly wetting fluid).

We first follow the shape of the drop during the spreading. The simulated spreading of the drop is shown in the form of contours of liquid phase volume fraction. Figure 4 depicts the simulated results of the drop contour at different time for two roughness heights ($h_r = 2.4$ and 50 μm). Note that the surface roughness cannot be displayed in the Fluent images. Each drop shows a similar evolution. After the contact with the solid surface, the initial shape of the drop is a part of a sphere and the drop behaves as a spherical cap with a circular base area. Then, the drop starts to spread and it is observed that the drop does not retain the form of an ideal spherical cap during the spreading. From the Figure, the temporal evolution of the shape of the drop becomes visible. The surface roughness has a certain influence on the drop shape during the spreading, since the roughness contributes to the pinning of the liquid/solid contact-line.[1,66] It is also interesting to note that the equilibrium shape of the drop is close to the final 'pancake', which is generally expected in the case of complete wetting.

In order to compare the shape of all drops during spreading it is more convenient to represent the 2D drop profile. Figure 5 illustrates the simulated time sequence

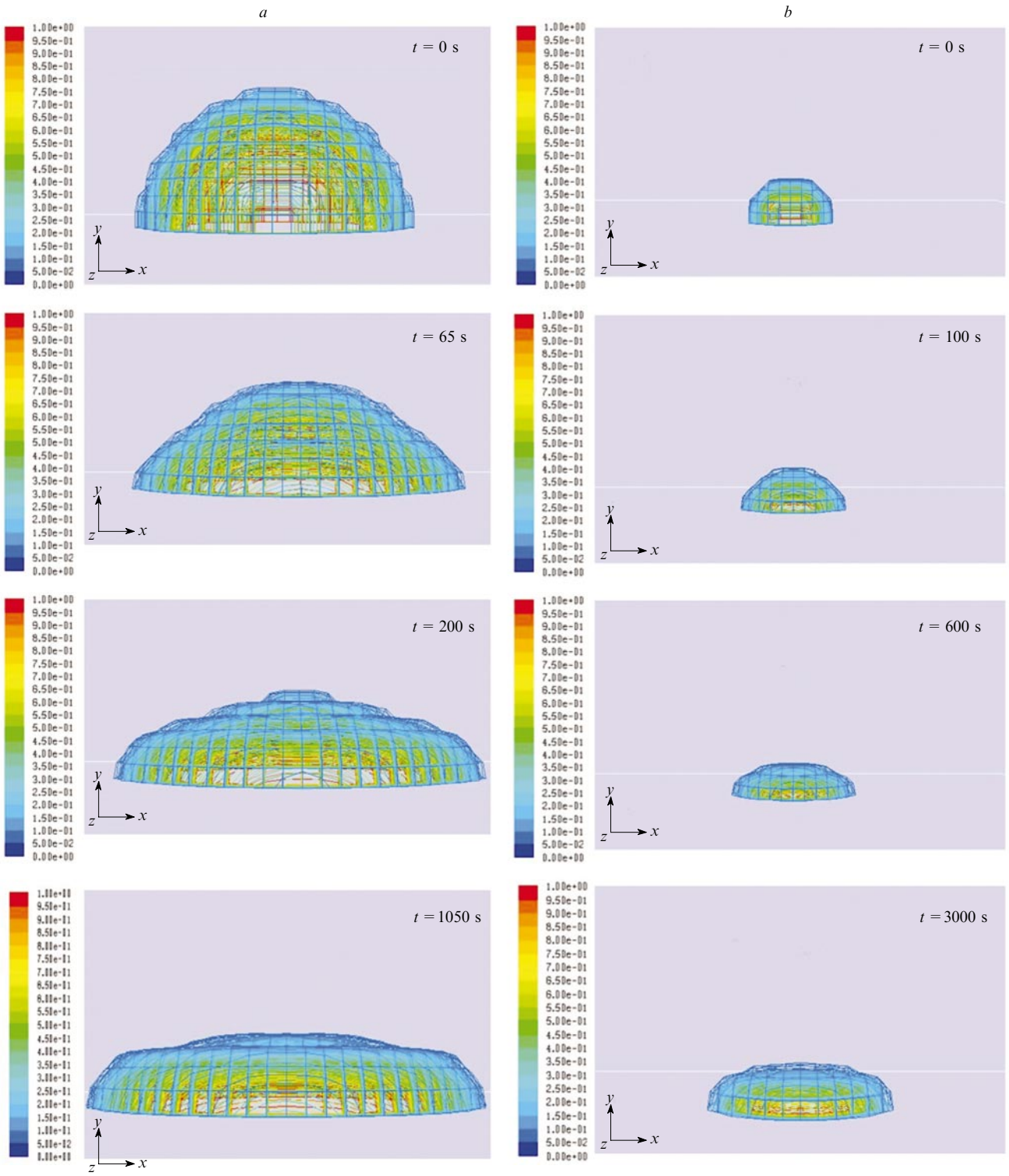


Figure 4. Simulated time sequence snapshots of a drop of silicone oil spreading on glass surface for roughness heights of: h_r = 50 μm (peak-to-peak distance = 12 μm) (*a*) and h_r = 2.4 μm (peak-to-peak distance = 0.4 μm) (*b*). Parameters used in calculations: γ = 24 mN m^{-1}, μ = 0.02 Pa s, drop volume V = 20 μl, $\Delta t = 2 \times 10^{-6}$ s and $\Delta x = 5 \times 10^{-4}$ mm.

snapshots of the 2D drop profile for different roughness sizes. The silicone oil drops show similar behaviour regardless of the roughness height. The successive stages of the spreading of a drop on a rough surface are visible. Initially, the drop spreads as a whole (see Fig. 5 *a* for t = 0.07 s) and the macroscopic cap of the drop sustains a capillary-dominated shape. After some time the 'foot' of liquid finds 'navigable channels' into the roughness and precedes a cap which feeds the foot (t = 100 – 500 s).[67] Some of the fluid spreads from the macroscopic edge into the roughness. It is assumed that the initial invasion process is the result of an 'essentially constant capillary force' pulling the fluid into

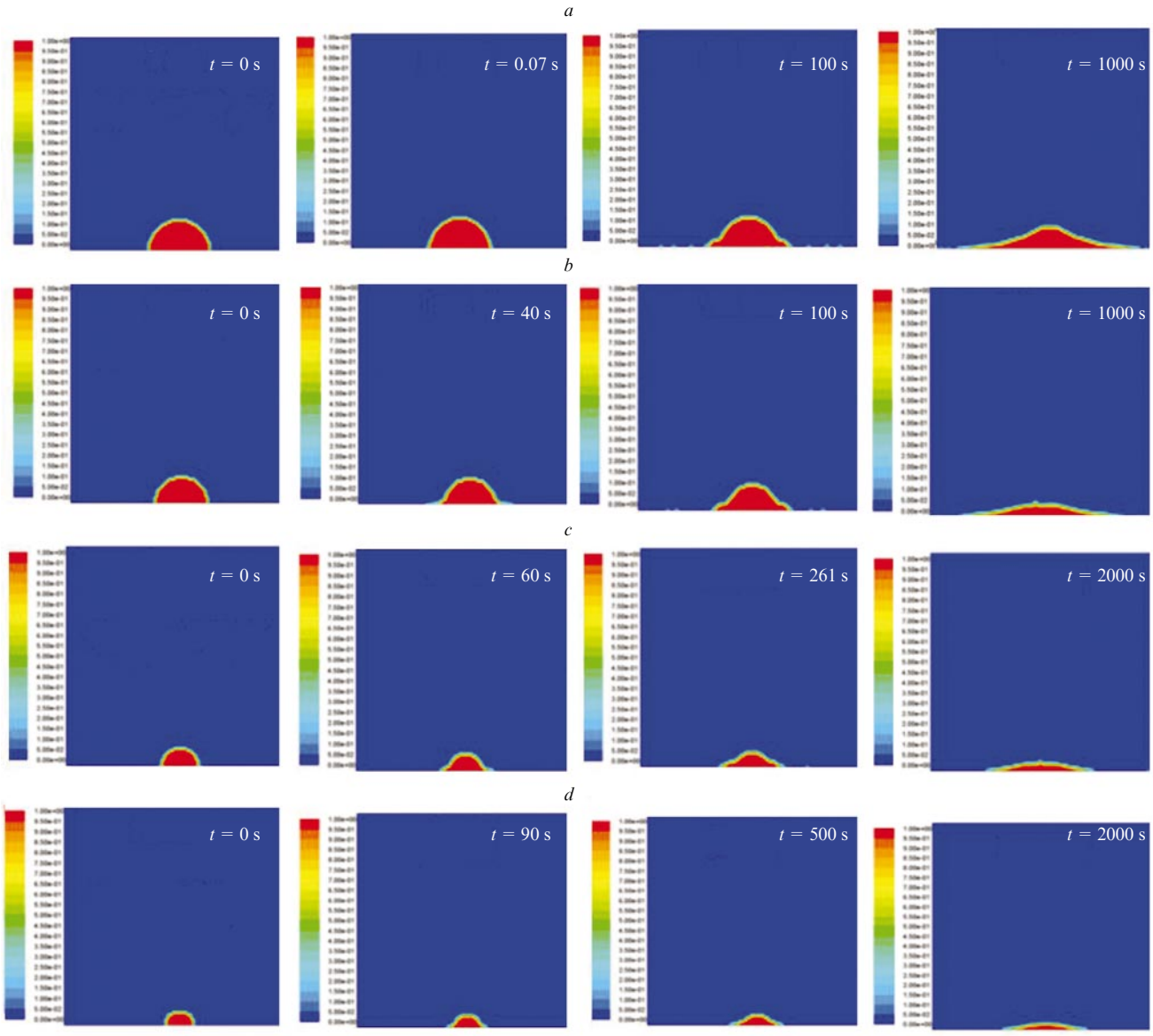


Figure 5. Simulated time sequence snapshots of the 2D drop profile of silicone oil spreading on glass surface at different roughness heights.
h_r and peak-to-peak distance /μm: 50 and 12 (*a*), 18 and 3.6 (*b*), 4.7 and 0.7 (*c*), 2.4 and 0.4 (*d*).
Parameters used in calculations: $\gamma = 24$ mN m^{-1}, $\mu = 0.02$ Pa s, $\Delta t = 2 \times 10^{-6}$ s and $\Delta x = 5 \times 10^{-4}$ mm.

the surface roughness.[22, 23] The liquid spreads in the roughness of the surface until it becomes consumed by troughs and valleys on the surface. When this reservoir is consumed, the drop again spreads as a whole ($t = 2000$ s) because the fluid in the macroscopic drop relaxes onto the fluid that had invaded the roughness. This confirms that the spreading of the liquid occurs by two modes: (i) on top of the rough surface and (ii) inside the capillary grooves, which make up the roughness (Wenzel state). The other important feature is that the final contact angles are very small. This confirms that the silicone oil completely wets the rough surface. Moreover, the drop spreads slowly since the contact angle is significantly reduced within some minutes. The numerical results cannot be directly compared with the experimental time sequence photographs under the same conditions since they are not displayed in the publications.[22, 23]

We examined more quantitatively the validity of the model by comparing the calculated and experimental radius as a function of time for a wide variety of surface roughness heights (Fig. 6). As expected, the radius increases with the time for all series. The calculated results compare well with the experimental data over a considerable temporal range (up to 140 000 s). The CFD approach accounts for almost all data points. Both the final drop radius and the subsequent dependence of the wetting are well described. This attests that the theory is valid for a very long period of time and also for large roughness heights ($h_r = 18$ and 50 μm). We have shown, using several independent numerical experiments, the validity of the model in the case where the invasion of the liquid into the roughness of the surface occurs (Wenzel state). This establishes that the theory takes into account the roughness invasion.

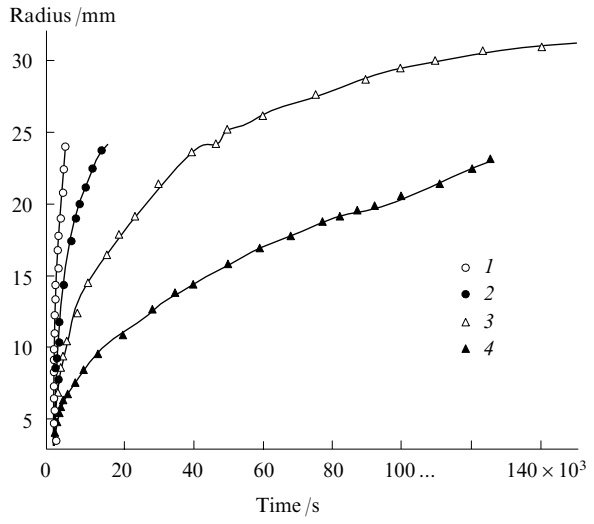


Figure 6. Comparison of the experimental (symbols, from Cazabat and Cohen Stuart [22]) and calculated (lines) time evolution of the drop radius of silicone oil on glass surface at different roughness heights.
h_r /μm: 50 (*1*), 18 (*2*), 4.7 (*3*), 2.4 (*4*).
Parameters used in calculations: $\gamma = 24$ mN m^{-1}, $\mu = 0.02$ Pa s, $\Delta t = 2 \times 10^{-6}$ s and $\Delta x = 5 \times 10^{-4}$ mm.

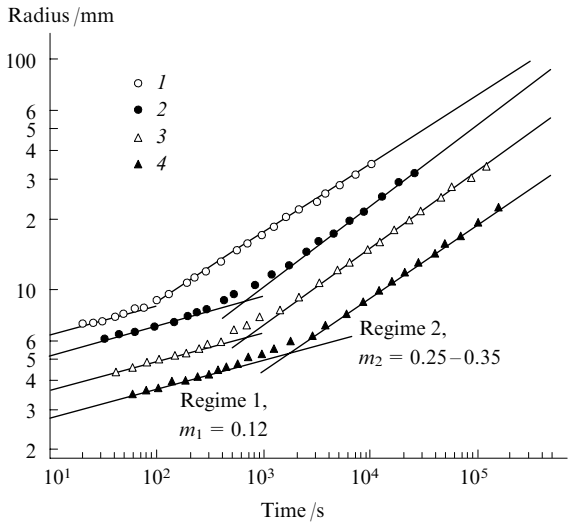


Figure 7. Calculated time evolution of the drop radius of silicone oil on glass surface at different roughness heights on a log-log scale (dots). Two distinguished parts of the curve are fit by linear regression (lines).
h_r /μm: 50 (*1*), 18 (*2*), 4.7 (*3*), 2.4 (*4*).

It was previously observed that several spreading regimes occurred during the time course of a drop on a rough surface. The succession of two different regimes was experimentally observed since the spreading followed two distinct power laws.[22, 23] The initial stage of the spreading process was very similar to this reported for smooth surface and the dependence of the drop radius R on time read as $R(t) \sim t^{1/8}$. Then, as the drop spreads, an important new regime appeared where part of the liquid spreads essentially in the roughness of the surface. This regime led to a power law of spreading with exponent values ranging from 0.25 to 0.4. The power law exponent value was close to 0.25 for large roughness height while it became equal to 0.4 for small roughness size. To validate the succession of these two regimes, the calculated drop radius has been plotted as a function of time on a log-log scale (Fig. 7) for several roughness sizes. The Figure has two successive linear segments. Each of these linear segments corresponds quite obviously to a particular spreading regime, and they are linked to one another by a non-linear stage corresponding to an intermediate situation. The linear increase in the drop radius on a log-log scale means that the corresponding spreading regime can be described by a power law of the form $R = K \times t^m$, where m and K are the two constant parameters depending on the experimental conditions but also on the time range. For each segment, the m_i and K_i parameters are optimized, the subscript i ($i = 1$ to 2) referring to the first and second linear sections. All the results are listed in Table 2. For the first regime, the power law exponents do not vary with the roughness size. The average m_1 value equals 0.125 ± 0.005. The power law exponents m_1 correspond well to theoretically predicted exponents corresponding to the 'smooth regime' ($m = 1/8$) for which the drop spreads on the top of the rough surface. In the second regime, the power law exponents depend on the roughness size. The values of m_2 vary with the roughness size. The values of m_2 are equal to 0.297, 0.332, 0.328 and 0.320 for roughness sizes of 50, 18, 4.7 and 2.4 μm, respectively. The power law exponents m_2 are in fair agreement with the exponents corresponding to the 'cap + foot' regime, for which the drop spreads inside the roughness, since the values of m_2 range from 0.25 to 0.4. In addition, the power law exponent value is close to 0.250 for roughness height of 50 μm. The model reproduces the experimentally determined 'smooth' and 'cap + foot' regimes. It is also important to note that the model successfully describes the non-linear stages (in a log-log scale) corresponding to intermediate situation between the spreading regimes. The CFD quantitative estimation of the evolution of the drop radius in the intermediate situation is necessary since it is not provided by the classical theory.

Table 2. Influence of the roughness height (h_r) on the calculated spreading parameters of silicone oil on glass surface.

h_r /μm	Regime 1		Regime 2	
	m_1	K_1 /mm s^{-m}	m_2	K_2 /mm s^{-m}
50	0.126	4.71	0.297	1.61
18	0.126	3.85	0.332	1.23
4.7	0.124	2.71	0.328	0.96
2.4	0.125	2.05	0.320	0.66

2. Spreading of vegetable and mineral oils on stainless steel

To test the validity of the model at a very short time (shorter than 3 s) and in the absence of liquid invasion, additional data from experiments performed with mineral and vegetable (coconut and palm) oils on stainless steel substrates are compared with the model. The experimental data were obtained by Narayan Prabhu and co-workers.[24] The surfaces of the stainless steel substrates were prepared using different grades of silicon carbide papers of various grit sizes to obtain surface roughness height (h_r) of

0.5 ± 0.02 μm, 1 ± 0.03 μm and 2 ± 0.04 μm, respectively. The corresponding peak-to-peak distances were 0.1, 0.3, and 0.5 μm, respectively.

Figure 8 depicts the simulated time sequence snapshots of the drop contour (2D drop profile) of palm oil spreading on stainless steel substrate at different roughness sizes. The results presented in the figure are fairly representative for the other results (coconut and mineral oils). The drops spread in a similar manner for all the roughness sizes. After the contact with the solid surface, the drop starts from an initial position with a contact angle of 85 to 70°. Then, the drop starts to spread since the contact angle reduces within some milliseconds. As the drop spreads, the drop height decreases while the drop radius increases. This process continues until the drop comes to the equilibrium position. From the Figure, the temporal evolution of the drop base radius and contact angle becomes visible. It is interesting to note that the drop retains the shape of an ideal spherical cap at any moment in time. This emphasizes that the liquid cannot fill inside the roughness. This confirms that the spreading of the drop occurs only on the top of the rough surface. The numerical results can be also compared with the experimental time sequence photographs under the same experimental conditions. Images in Fig. 8 are in good

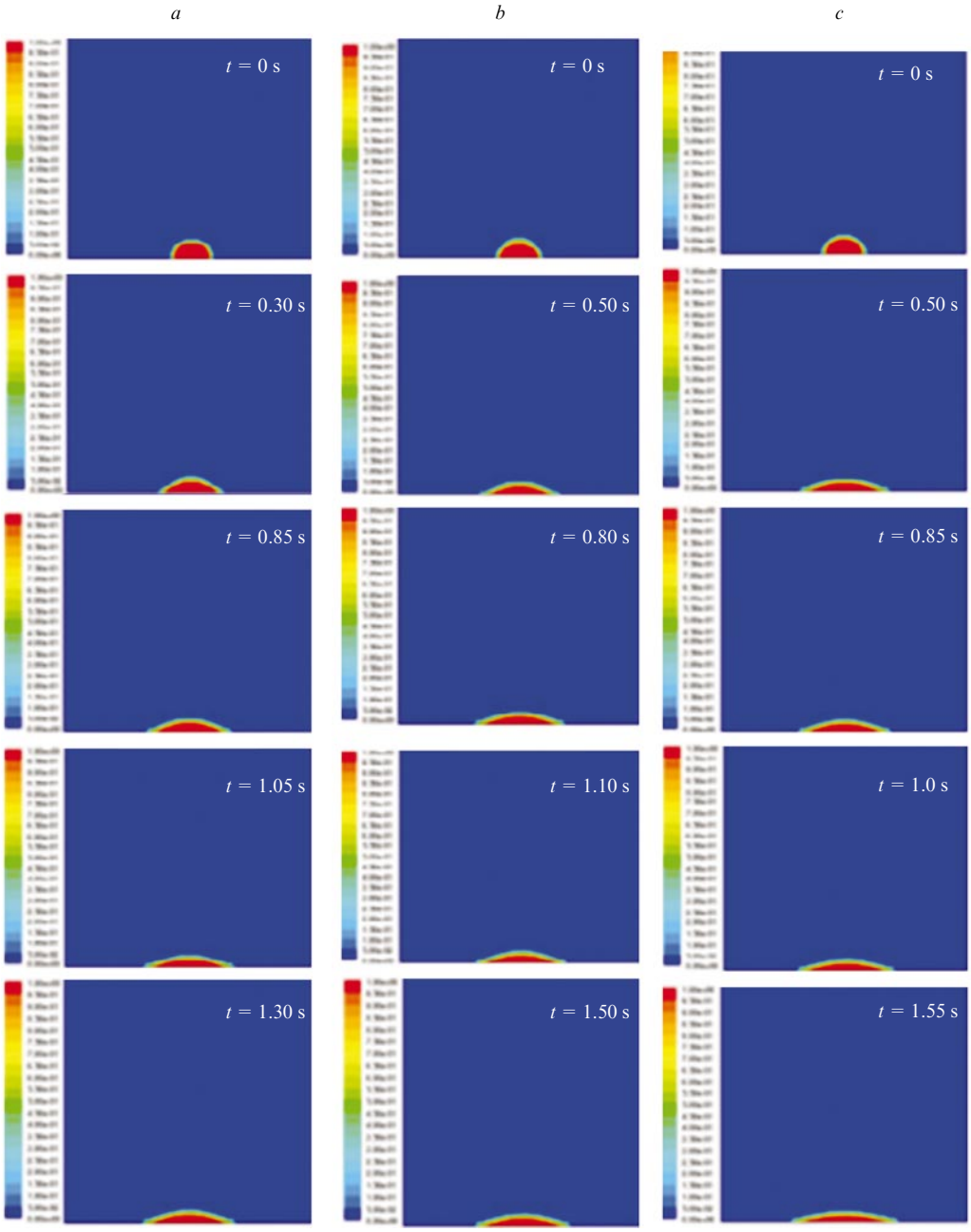


Figure 8. Simulated time sequence snapshots of the 2D drop profile of palm oil spreading on stainless steel substrate at different roughness heights. h_r/μm: 0.5 (*a*), 1 (*b*), 2 (*c*).
Parameters used in calculations: $\gamma = 33.8$ mN m^{-1}, $\mu = 0.07$ Pa s, $\Delta t = 10^{-5}$ s and $\Delta x = 5 \times 10^{-4}$ mm.

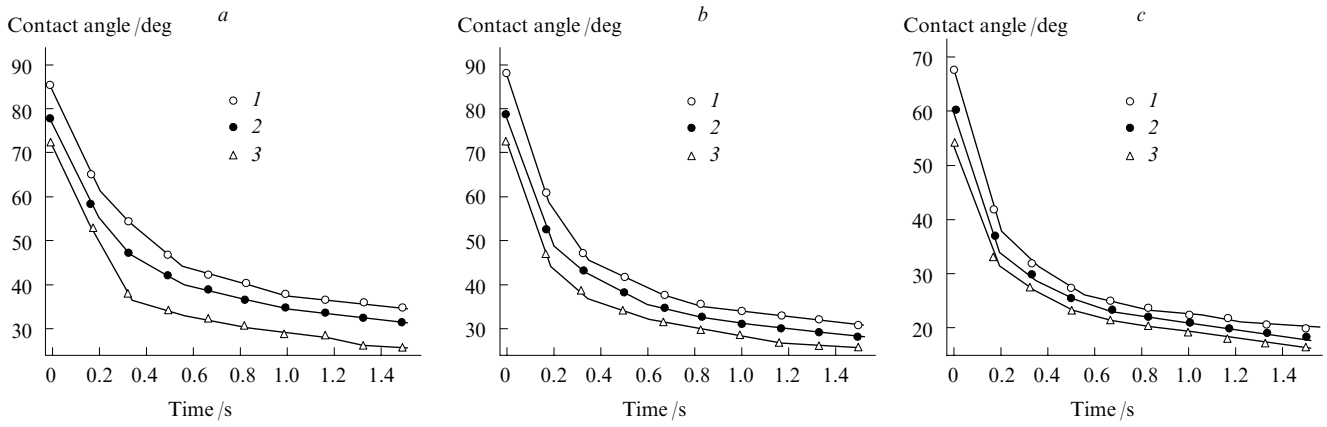


Figure 9. Comparison of the experimental (dots, from Narayan Prabhu *et al.*[24]) and calculated (lines) time evolution of the dynamic contact angle of various oils on stainless steel substrate at different roughness heights: mineral oil, $\gamma = 30.0$ mN m^{-1}, $\mu = 0.08$ Pa s (*a*), palm oil, $\gamma = 33.8$ mN m^{-1}, $\mu = 0.07$ Pa s (*b*), coconut oil: $\gamma = 29.4$ mN m^{-1}, $\mu = 0.03$ Pa s.
h_r /μm: 0.5 (*1*), 1 (*2*), 2 (*3*). Parameters used in calculations: $\Delta t = 10^{-5}$ s and $\Delta x = 5 \times 10^{-4}$ mm.

agreement with the images reported by Narayan Prabhu and co-workers.[24]

We examined more precisely the validity of the model by comparing the calculated and experimental dynamic contact angle as a function of time for a wide variety of oils and roughness sizes (Fig. 9). All the oils show the same trend. As expected, the calculated dynamic contact angle decreases with the time for all the oils and roughness sizes. The oil starts spreading rapidly at a relatively high velocity resulting in a sharp decrease of the contact angle. However, within a very short period of time, the spreading rate diminishes significantly to almost zero indicating the stabilization of the contact angle. This is due to the attainment of equilibrium between the various surface forces under action. Further relaxation of the contact angle is negligible. Note that the contact angle reaches an equilibrium value significantly larger than 0° ($\sim 20 - 40^\circ$). This means that the oils do not wet the solid completely and indicates that we discuss the motion of the contact-line under conditions of partial wetting. A very good agreement between the model and experimental data is found. The CFD approach accounts for almost all data points. Both the final contact angle and the subsequent dependence of wetting are well reproduced. This confirms that the model describes perfectly the temporal evolution of the contact angle. The roughness size has a weak effect on the kinetics of spreading in the range of roughness heights studied (0.5 – 2 μm). The time of drop relaxation does not significantly vary with the roughness height. It is also interesting to note that the equilibrium contact angle decreases with the roughness size. This is in perfect agreement with the Cassie's and also Wenzel's assumptions. These two models are used for correcting the contact angle variations caused by the solid surface roughness under static conditions in the equilibrium state. Depending on the relative magnitude of the roughness of the surface and the size of the liquid drop, the surface roughness affects the contact angle in two distinct ways. One is due to the increased solid/liquid contact area (Wenzel approach), the other is due to the reduced contact area (Cassie model). In the Wenzel model, the increase in the surface area is taken into account. A rough surface provides an additional interfacial area for the spreading liquid which results in an increase of the surface energy. Contact angle variation due to increased contact area is generally modelled by the Wenzel equation [68]

$$\cos\theta^* = r\cos\theta \tag{15}$$

where θ^* is the equilibrium apparent contact angle of a liquid drop on a rough surface, θ is the equilibrium contact angle on a smooth surface made of the same material, and r is the average roughness ratio, *i.e.*, the factor by which the roughness increases the solid/liquid interfacial area. The Wenzel equation is based on the assumption that the liquid completely penetrates into the roughness. However, for many real rough surfaces, air may be trapped in asperities on surface by the liquid drop. Under this circumstance the Wenzel model is not applicable.

In a situation where the liquid drop does not make full contact with the substrate due to surface roughness, the Cassie model links the apparent contact angle to the intrinsic contact angles of the substrate [69]

$$\cos\theta^* = f_1\cos\theta_1 - f_2 \tag{16}$$

where f_1 is the fraction of the surface that contacts the liquid drop with a contact angle of θ_1 and f_2 is the fraction of surface that has no contact with the liquid drop. Equation (16) shows the Cassie model for a simple rough surface with only one surface chemistry.

When the composite surface consists of a solid surface and an air layer, Eqn (16) becomes [21]

$$\cos\theta^* = f(\cos\theta + 1) - 1 \tag{17}$$

where f is the fraction of the solid area.

The applicability of the Wenzel model and the Cassie model is easily verified by plotting $\cos\theta^*$ with respect to $\cos\theta$. The $\cos\theta$ values were found using experimental data previously obtained by Narayan Prabhu *et al.*[24] upon application of some mineral and vegetable oils onto smooth stainless steel substrate. According to Eqns (15) and (17), $\cos\theta^*$ is expected to depend linearly on $\cos\theta$. If the results come close to a straight line that passes the origin, this will

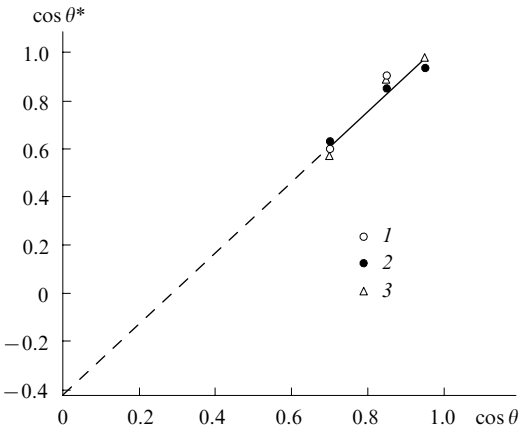


Figure 10. Relationship between the cosine of the equilibrium contact angle θ^* on the rough stainless steel surface and the cosine of the equilibrium contact angle θ on the reference smooth surface. The line represents the best linear fit given by $\cos\theta^* = 1.43\cos\theta - 0.39$ ($R^2 = 0.94$). The dashed line is drawn to guide the eyes.
h_r/μm: 0.5 (*1*), 1 (*2*), 2 (*3*).

suggest that the change in the contact angle due to the roughness is explained well by the Wenzel model. On the contrary, if the straight line does not cross the origin, this will indicate that the contact angle modification due to the roughness is described by the Cassie model. In Fig. 10, the reported cos θ^* from the data of Fig. 9 are plotted against cos θ for palm, coconut and mineral oils. The data points for the various oils fall on a single line indicating that cos θ^* increases linearly with cos θ. However, the straight line does not pass the origin, the intercept being -0.4. This result is in perfect agreement with Eqn (17). This confirms that the oil drop contact with the sized rough stainless steel surfaces can be described using the Cassie equation. The solutions partially wet the side walls of the roughness but do not drop onto the bottom of the rough structure, leaving an air layer between the solution and the surface roughness. Therefore, the simulations suggest that Cassie's law holds for weak surface roughness, provided that very few or no significant contact-line pinning occurs.

The time evolution of the drop base radius is also analyzed to confirm the ability of the model to reproduce the experimental spreading on rough surfaces. We compare the temporal evolution of the calculated and experimental radius in three experimental cases (palm, mineral and coconut oils on a stainless steel substrate of roughness size equal to $h_r = 2$ μm) which are quite typical and which have been selected to illustrate the model (Fig. 11). The Figure indicates that the model is able to satisfactorily describe the temporal evolution of the drop base radius. The different wetting properties including the drop base radius and the dynamic contact angle can be successfully simulated. The theory remains valid at very short time, *i.e.*, 1.4 s (Fig. 9) and 3 s (Fig. 11). This is a very important result since the wetting behaviour is significantly affected during the initial stage of spreading. Both, the contact angle relaxation and the increase in the drop base radius are sharp. The model captures the essential physics of the initial stage of wetting when the oils spread rapidly, on the top of the rough surface, at a relatively high velocity.

Due to the high degree of correspondence for a wide variety of configurations, the model can be used to predict the spreading behaviour as a function of the roughness size. Figure 11 shows the calculated radius as a function of the time for various oils and roughness sizes. The time evolution of the drop is significantly affected by the roughness size. The wetting velocity increases with the size of the roughness since the curves become somewhat steeper. Consequently, the radius relaxation extends longer on low rough surface before attaining equilibrium. In addition, the final radius increases with the roughness height. As expected, the oil viscosity plays a role in the speed of the motion of the oil drop. Coconut oil shows rapid flow behaviour while the kinetics of spreading of mineral and palm oils are slower. The viscosity values for these oils are significantly different. Coconut oil has the lowest viscosity ($\mu = 0.03$ Pa s) and, therefore, spread faster. On the contrary, viscosities of palm and mineral oils are higher and

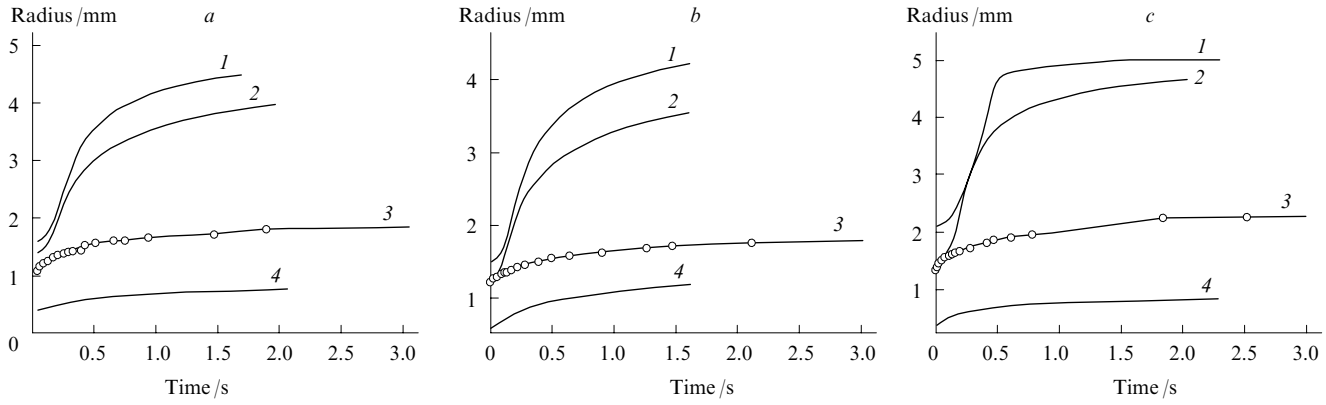


Figure 11. Calculated radius as a function of time of various oils on stainless steel substrate at different roughness heights: mineral oil, $\gamma = 30.0$ mN m^{-1}, $\mu = 0.08$ Pa s (*a*), palm oil, $\gamma = 33.8$ mN m^{-1}, $\mu = 0.07$ Pa s (*b*), coconut oil: $\gamma = 29.4$ mN m^{-1}, $\mu = 0.03$ Pa s.
The experimental results, from Narayan Prabhu *et al.*,[24] corresponding to the spreading of mineral, coconut and palm oils on stainless steel surface of roughness height equal to $h_r = 2$ μm (dots) are also shown for comparison. h_r/μm: 10 (*1*), 5 (*2*), 2 (*3*), 1 (*4*).
Parameters used in calculations: peak-to-peak distance of 0.5 μm, $\Delta t = 10^{-5}$ s and $\Delta x = 5 \times 10^{-4}$ mm.

comparable ($\mu = 0.08$ Pa s for mineral oil and $\mu = 0.07$ Pa s for palm oil) resulting in slow spreading. This establishes that the theory takes into account the change of the liquid viscosity. The CFD estimation of the evolution of the drop radius for different viscosities is necessary since the dynamics of spreading is modified by the viscosity. The accuracy of the model results demonstrate that the influence of the physicochemical properties of the liquid such as viscosity can be successfully simulated on a rough surface.

VI. Conclusion

The dynamics of drop spreading, for time periods longer than 10^5 s, of mineral, vegetable and silicone oils on rough surfaces can be readily described by a computational fluid dynamics model applying the volume of fluid method to the case of a drop previously deposited on a surface. The model has been implemented to simulate the time evolution of the drop base radius and contact angle. The simulation takes into account the surface tension and wall adhesion phenomenon. The surface roughness is introduced in the simulation as an equivalent sand-grain roughness. The surface roughness is characterized by two parameters: the average roughness height and the peak-to-peak distance. The use of wall functions is required for near-wall modeling inside the roughness in order to allow the penetration of the liquid inside the roughness. This type of roughness modification is currently present in many CFD codes. The only adjustable parameter is the initial conditions of simulation (initial drop radius and initial time) which has to be identical to those of the experiments.

The simulations are quantitatively compared with experimental data reported by other research groups. The oil nature (silicone, mineral, coconut and palm), surface roughness and type of surface (glass and stainless steel) have been varied. The calculated results are in good agreement with experimental data for a large range of oils and surfaces. The fact that we obtain a good agreement between the proposed theory and the experimental values for time periods exceeding 10^5 s is a very strong argument in favour of the model. We have also shown that the two physical mechanisms responsible for liquid spreading on rough surface, *i.e.*, on the top of the rough surface (Cassie state) and/or inside the roughness (Wenzel sate) can be successfully simulated.

The simulations emphasize the rich set of behaviours that can be obtained when varying the roughness height and the wetting properties of the liquid. On the one hand, in the case of drops of silicone oil spreading on glass surfaces ($h_r = 2.4 - 50$ μm and peak-to-peak distance of $0.4 - 12$ μm), for which the spreading of the liquid occurs on the top of the roughness and inside the roughness, the numerical results reproduce perfectly the several spreading regimes which occur during the time course of the drop. The number and the nature of the regimes are not affected by the roughness size. The succession of a gravity regime [$R(t) \sim t^{1/8}$] and lastly a fast regime [$R(t) \sim t^{0.29-0.34}$] is demonstrated. The CFD approach is able to specify the kinetic regime associated with the different mode of energy dissipation during the drop shape transformation and also the time window in which each particular regime holds preferentially. On the other hand, the dynamics of drop spreading of vegetable and mineral oils on stainless steel surfaces ($h_r < 2.5$ μm and peak-to-peak distances < 0.5 μm) occurs on the top of the roughness and the oil drop contact with the surface can be described using the Cassie equation. The accuracy of the model results establishes also that the influence of the liquid viscosity can be successfully simulated on a rough surface.

References

1. P G de Gennes *Rev. Mod. Phys.* **57** 827 (1985)
2. D Bonn, J Eggers, J Indekeu, J Meunier, E Rolley *Rev. Mod. Phys.* **81** 739 (2009)
3. T D Blake *J. Colloid Interface Sci.* **299** 1 (2006)
4. T Roques-Carmes, V Mathieu, A Gigante *J. Colloid Interface Sci.* **344** 180 (2010)
5. M N Popescu, G Oshanin, S Dietrich, A-M Cazabat *J. Phys.: Condens. Matter* **24** 243102 (2012)
6. C W Hirt, B D Nichols *J. Comput. Phys.* **39** 201 (1981)
7. N Rajabi, A Dolatabadi *Colloids Surf., A* **365** 230 (2010)
8. J Fukai, Y Shiiba, T Yamamoto, O Miyatake, D Poulikakos, C M Megaridis, Z Zhao *Phys. Fluids* **7** 236 (1995)
9. J Xiao, S Chaudhuri *Langmuir* **28** 4434 (2012)
10. S F Lunkad, V V Buwa, K D P Nigam *Chem. Eng. Sci.* **62** 7214 (2007)
11. B A Nichita, I Zun, J R Thome, in *The Proceedings of the 7th International Conference on Multiphase Flow, Tampa, FL, 2010* p. 1
12. B A Nichita, Ph.D. Thesis École Polytechnique Fédérale de Lausanne, Switzerland, 2010
13. P R Gunjal, V V Ranade, R V Chaudhari *AIChE J.* **51** 59 (2005)
14. P R Gunjal, V V Ranade, R V Chaudhari *Catal. Today* **79** 267 (2003)
15. H Alla, S Freifer, T Roques-Carmes *Colloids Surf., A* **386** 107 (2011)
16. D Natarajan, H Hangan, in *The Proceedings of the 11th Americas Conference on Wind Engineering, San Juan, Puerto Rico, 2009* p. 81
17. B Blocken, T Stathopoulos, J Carmeliet *Atmos. Environ.* **41** 238 (2007)
18. J B Lee, S H Lee *Langmuir* **27** 6565 (2011)
19. S Semal, T D Blake, V Geskin, M J de Ruijter, G Castelein, J De Coninck *Langmuir* **15** 8765 (1999)
20. J Léopoldès, D G Bucknall *J. Phys. Chem. B* **109** 8973 (2005)
21. J Bico, C Tordeux, D Quéré *Europhys. Lett.* **55** 214 (2001)
22. A M Cazabat, M A Cohen Stuart *J. Phys. Chem.* **90** 5845 (1986)
23. A M Cazabat, M A Cohen Stuart *Prog. Colloid Polym. Sci.* **74** 69 (1987)
24. K Narayan Prabhu, P Fernades, G Kumar *Mater. Design* **30** 297 (2009)
25. L Xu, H Fan, C Yang, W M Huang *J. Colloid Interface Sci.* **323** 126 (2008)
26. D Kannangara, W Shen *Colloids Surf., A* **330** 151 (2008)
27. G Kumar, K Narayan Prabhu *Adv. Colloid Interface Sci.* **133** 61 (2007)
28. J Harting, C Kunert, H J Herrmann *Europhys. Lett.* **75** 338 (2006)
29. H Huang, D T Thorne Jr , M G Schaap, M C Sukop *Phys. Rev. E* **76** 066701 (2007)
30. S Mukherjee, J Abraham *J. Colloid Interface Sci.* **312** 341 (2007)
31. R Benzi, L Biferale, M Sbragaglia, S Succi, F Toschi *Phys. Rev. E* **74** 021509 (2006)
32. R Benzi, L Biferale, M Sbragaglia, S Succi, F Toschi *Europhys. Lett.* **74** 651 (2006)
33. P Raiskinmaki, A Shakib-Manesh, A Jësberg, A Koponen, J Merikoski, J Timonen *J. Stat. Phys.* **107** 143 (2002)
34. D R Heine, G S Grest, E B Webb III *Phys. Rev. E* **68** 061603 (2003)

35. D R Heine, G S Grest, E B Webb III *Phys. Rev. E* **70** 011606 (2004)
36. G Martic, F Gentner, D Seveno, D Coulon, J De Coninck, T D Blake *Langmuir* **18** 7971 (2002)
37. G Martic, F Gentner, D Seveno, J De Coninck, T D Blake *J. Colloid Interface Sci.* **270** 171 (2004)
38. P A Thompson, M O Robbins *Phys. Rev. Lett.* **63** 766 (1989)
39. F Gentner, G Ogonowski, J De Coninck *Langmuir* **19** 3996 (2003)
40. M Sbragaglia, R Benzi, L Biferale, S Succi, F Toschi *Phys. Rev. Lett.* **97** 204503 (2006)
41. M N Popescu, S Dietrich, G Oshanin *J. Phys.: Condens. Matter* **17** S4189 (2005)
42. F Diotallevi, L Biferale, S Chibbaro, G Pontrelli, F Toschi, S Succi *Eur. Phys. J. ST* **171** 237 (2009)
43. D Dimitrov, A Milchev, K Binder *Phys. Rev. Lett.* **99** 054501 (2007)
44. S Chibbaro, E Costa, D I Dimitrov, F Diotallevi, A Milchev, D Palmieri, G Pontrelli, S Succi *Langmuir* **25** 12653 (2009)
45. J U Brackbill, D B Kothe, C Zemach *J. Comput. Phys.* **100** 335 (1992)
46. J Li *C. R. Acad. Sci., Ser. IIb* **320** 391 (1995)
47. M Meier, G Yadigaroglu, B L Smith *Eur. J. Mech. B: Fluids* **21** 61 (2002)
48. S F Kistler, in *Wettability* (Ed. J C Berg) (New York: Marcel Dekker, 1993) p. 311
49. L Bocquet, J-L Barrat *Soft Matter* **3** 685 (2007)
50. C Sendner, D Horinek, L Bocquet, R R Netz *Langmuir* **25** 10768 (2009)
51. C Kunert, J Harting, O I Vinogradova *Phys. Rev. Lett.* **105** 016001 (2010)
52. O I Vinogradova, A V Belyaev *J. Phys.: Condens. Matter* **23** 184104 (2011)
53. O I Vinogradova, A L Dubov *Mendeleev Commun.* **22** 229 (2012)
54. D Quéré *Annu. Rev. Mater. Res.* **38** 71 (2008)
55. E Bonaccurso, H-J Butt, V S J Craig *Phys. Rev. Lett.* **90** 144501 (2003)
56. S Granick, Y Zhu, H Lee *Nat. Mater.* **2** 221 (2003)
57. A Mongruel, T Chastel, E S Asmolov, O I Vinogradova *Phys. Rev. E* **87** 011002 (2013)
58. R M Patrikar *Appl. Surf. Sci.* **228** 213 (2004)
59. T Provder, B Kunz *Prog. Org. Coat.* **27** 219 (1996)
60. E Lauga, M P Brenner, H A Stone, in *Hanbook of Experimental Fluid Mechanics* (Eds C Tropea, A L Yarin, J F Foss) (New York: Springer, 2007) p. 1219
61. M Renardy, Y Renardy, J Li *J. Comput. Phys.* **171** 243 (2001)
62. S Afkhami, S Zaleski, M Bussmann *J. Comput. Phys.* **228** 5370 (2009)
63. F Schönfeld, S Hardt *Comput. Fluids* **38** 757 (2009)
64. J A Moriarty, L W Schwartz *J. Eng. Math.* **26** 81 (1992)
65. O Weinstein, L M Pismen *Math. Model. Nat. Phenom.* **3** (1) 98 (2008)
66. D Kannangara, H Zhang, W Shen *Colloids Surf., A* **280** 203 (2006)
67. M Apel-Paz, A Marmur *Colloids Surf., A* **146** 273 (1999)
68. R N Wenzel *Ind. Eng. Chem.* **28** 988 (1936)
69. A B D Cassie, S Baxter *Trans. Faraday Soc.* **40** 546 (1944)